Scalable and Multifunctional Carbon Nanotube-Based Textile as Distributed Sensors for Flow and Cure Monitoring

Hongbo Dai[1] and Erik T. Thostenson[1,2,3*]

[1]Center for Composite Materials, [2]Department of Mechanical Engineering, and [3]Department of Materials Science and Engineering, University of Delaware, Newark, Delaware 19716, United States

ABSTRACT

Many manufacturing processes involve flow and cure of polymeric materials and development of sensors to detect these phenomena *in situ* and in real-time is important to reduce processing time and improve quality. This paper reports the development of a novel multifunctional sensor where carbon nanotubes are deposited onto a nonwoven textile to create a thin and porous areal sensor. The sensor is produced using a scalable dip-coating process and carbon nanotubes form an electrically conductive network on the fabric. Vacuum assisted resin transfer molding (VARTM) for advanced fiber composites is used to validate the sensor by using global and local distributed measurements to monitor the flow of epoxy resin. Spatial flow mapping is demonstrated using electrical impedance tomography (EIT). In a series of 2-D radial flow experiments, the EIT maps demonstrate accurate estimations for the resin flow, in terms of flow front location and shape, and is able to pinpoint dry spots and unsaturated regions. During elevated temperature cure, the sensor electrical response can be correlated directly to changes in viscosity and gelation of the epoxy. The sensor offers potential as a process sensor for flow and cure as well as for structural health monitoring.

1. Introduction

Advanced fiber composites are increasingly used in a wide variety of applications, including aerospace, shipbuilding, automobile, and civil industries, because of their high specific modulus and strength, excellent corrosion and impact resistance, and improved fatigue strength [1-4]. Liquid molding processes, such as resin transfer molding (RTM), are increasingly popular composites manufacturing processes because they can be automated and are less labor intensive than conventional manual lay-up processes. In the RTM process a liquid thermosetting polymeric resin, such as epoxy or vinyl ester, is injected into a dry fibrous preform [2, 5]. A variation on this process, known as vacuum-assisted RTM (VARTM), where vacuum applied through the vent line compacts the preform, removes the air in the cavity, and infuses the resin into the preform, is often used to manufacture large-scale composite structures due to its net-shape manufacturing capability

* Corresponding author.
Tel: 302 831-8789.
E-mail address: thosten@udel.edu (Erik T. Thostenson)

and cost-effectiveness [6]. The formation of defects during the manufacturing process can significantly impact the mechanical performance of the composite, and quality assurance is of critical importance for composite manufacturers to guarantee structural reliability. Therefore, the occurrence of process-induced defects, such as dry spots, unsaturated zones, and insufficient cure, must be detected at early stages of the manufacturing process, and there is a critical need for on-line, in situ processes for monitoring that can be coupled with process control systems to minimize part scrap and repair [7-9].

Conventional methods using point and linear sensors have been investigated for monitoring composites manufacturing processes. Digital cameras [10, 11] are often used to capture the resin flow front in real time, but they are not applicable in case of nontransparent, closed molds. Point sensors such as thermocouples [12], pressure transducers [13], fiber-optics [14, 15], resistive sensors [16-18], and dielectric/capacitive sensors [19-21] have been employed to detect the resin flow front locations *in situ* during resin impregnation. In particular, electrical sensors [16, 19, 22] and fiber-optic sensors [23, 24] have been utilized to monitor the resin cure cycle by measuring the curing reaction-induced conductivity/permittivity and optical property variations, respectively. However, these point sensors can only detect local responses. Line-type sensors, such as the linear conductor sensors [17, 25], optical fiber Bragg grating sensors [15, 24], and the electric time-domain reflectometry sensors [26], can detect resin arrival at distributed points along the length of sensing lines, enabling one-dimensional (1-D) sensing along the sensor. Traditionally, 2-D areal sensing has been achieved using the arrays of distributed point sensors [19, 27] and the grids of line sensors – such as the SMARTweave system [28, 29]. Since the array/grid density determines the detection accuracy, a sensing network with high coverage requires a large number of sensors which can result in complex and costly implementation. Also, embedded sensors are invasive to the composite structure, which can initiate defects.

Recent advances in nanostructured carbon has enabled new pathways to develop high performance and minimally intrusive sensors for process monitoring because of the structure-dependent electrical properties of the sensing networks formed by nanomaterials [30-34]. In a pilot study, Zhang and co-workers [35] coated carbon nanotubes (CNTs) onto a short, individual glass fiber using an electrophoretic deposition approach and utilized the coating as an interphase sensor to monitor polymer chemical and physical transitions *in situ*. The working principle of the sensor is that the coating of discontinuous CNTs forms an electrically conductive network and the CNT-

CNT electrical tunneling is altered by nearby polymer transitions, resulting in electrical resistance changes of the interphase. Similarly, Luo and Liu [33] spray-coated graphite nanoplatelets (GNPs) onto a glass filament to form a GNP-fiber sensor that was embedded into a composite laminate and used to monitor the epoxy curing process, where a sensor gain factor of ~186% resistance change was observed. In addition, Lu *et al.* [36] used a 3×1 cm^2 buckypaper (a high-density CNT sheet) sensor and placed it in a 16-ply epoxy/glass prepreg laminate. During the cure cycle, the sensor showed an overall gain factor of ~240% and its resistive response was able to identify the key resin phase changes such as the lowest viscosity and gel point.

Luo *et al.* [37] and Wang *et al.* [38] created line sensors that were 15 cm long using glass fiber bundles coated with CNT and reduced graphene oxide (rGO) which were integrated in a fabric to create a continuous 1-D sensing line. During the VARTM process, the resistive response of the sensors enabled tracking of the resin flow front along the sensing line [37] and detect resin gelation and curing [37, 38]. The highest gain factor of ~1600% was demonstrated by the CNT-fiber sensors [38]. Additionally, Luo and co-workers [39] developed a 15×15 cm^2 area sensor using a 5×5 grid of CNT-fiber sensors, which demonstrated the capability of mapping spatial resin flow but with low resolution. Gnidakouong *et al.* [40] and Ali *et al.* [41] deposited CNTs and rGO, respectively, to form fabric sensors in sizes of 15×15 and 40×10 cm^2 that were exploited to monitor the VARTM process. Both area sensors showed improved coverage compared to point [36], line [33, 37, 38], and grid [39] sensors, and they displayed gain factors of ~160% [40] and ~30% [41]. However, due to the simple two-electrode sensing scheme employed in references those sensors responses only provided the averaged global information over the sensing area. Although all of the above-mentioned nanomaterial-based sensors can realize *in situ* and on-line monitoring of composite manufacturing process, the potential high cost – due to the complex synthesis of base materials and implementations – and limited sensing capabilities may hinder progress towards practical applications.

In this paper, we report a distributed large-area CNT-based textile fabric sensor and explore its capability for *in situ* full-field monitoring of the VARTM process. This 400 μm thick sensor consists of a nonwoven carrier fabric of glass fibers with a CNT nanocomposite coating deposited onto the fiber surface using a straightforward dip-coating approach, which establishes a continuous resistive network that is highly sensitive to physical and chemical occurring in all stages of the VARTM process. In 1-D flow experiments, the real-time electrical response of the sensor can

detect applied vacuum pressure, resin flow progression, and resin phase changes during cure with a bulk gain factor of ~90%. Compared with the bulk resistive response, the distributed sensing regions partitioned from a continuous sensor show a more immediate and distinguishable response to the local resin flow progression.

Electrical impedance tomography (EIT) is a noninvasive imaging approach that has been being investigated in the geophysical and biomedical societies since the mid-1980s [42-44]. EIT reconstructs the spatial conductivity distribution within an electrically conductive medium based on boundary voltage measurements resulting from a series of electrical current injections [42-44]. Over the past few years, an active research area has emerged on the applications of EIT to the self-sensing composites as a nondestructive imaging tool for damage sensing and identification [45-49], pressure mapping [50,51], and structural health monitoring (SHM) [52-54]. For instance, Tallman and Wang [47] developed a sine wave constrained EIT method and subsequently demonstrated its applications on a 54 mm × 54 mm carbon nanofiber (CNF)/epoxy composite plate, a 101 mm × 152 mm carbon black (CB)-filled fiberglass laminate, and a 25.4 mm × 25.4 mm CNF/polyurethane composite sample for mapping the hole damage, impact damage, and distributed strain, respectively. In addition to the applications on planar structures, Thomas *et al*. [49] implemented EIT on a circular tube consisted of the CB-modified fiberglass composite (in diameter of 66.2 mm and length of 132.4 mm) for impact damage detection. In addition, EIT-based sensing layers have been developed and applied to nonconductive structures for damage evaluation [45] and SHM [53]. Smyl and co-workers [53] coated a conductive silver paint onto a cement mortar beam surface with a size of 508 × 152 mm and used 28 boundary electrodes to form a EIT-based sensor. They adopted a nonlinear difference imaging algorithm and showed its capability of mapping the complex cracking patterns developed on the beam surface under increasing three-point bending loads. Additionally, a successful attempt at EIT-based damage detection in electrically anisotropic carbon fiber-reinforced polymer composites has been reported by Cagan *et al*. [48] using a Gaussian anisotropic algorithm. Recently, Fan and co-workers [55] developed an electrical capacitance tomography approach with an eight-electrode circular sensing system (120 mm in diameter) and a Gauss-Newton iterative algorithm and examined it for monitoring cure in CNT/epoxy nanocomposites. This sensing method was able to map the evolution of the relative permittivity change in nanocomposite samples under different curing time.

For the first time, electrical impedance tomography (EIT) has been successfully integrated with this CNT-based fabric sensor during VARTM process to offer true 2-D resin flow mapping capability. Here, the random, nonwoven structure of the fabric results in globally isotropic electrical properties, so the CNT-based sensor can be treated as an effective EIT domain to enable reconstructions of the conductivity distribution across the sensor area. During the infusion process, the insulating epoxy resin drastically decreases the local electrical conductivity of the fabric by disrupting the carbon nanotube network, enabling the spatial detection of resin flow using EIT. In four 2-D radial flow case studies, the EIT maps of resin flow-induced conductivity changes demonstrate accurate estimations for the flow evolution, with respect to the flow front locations and shape, and closely pinpoint local problematic dry spots and unsaturated zones. Our prior research has investigated this type of CNT-based textile as a piezoresistive sensor for structural monitoring and damage sensing [45,56,57]. This type of sensor may be utilized as a tool-mounted sensor that could be removed from the composite after manufacturing but it also offers potential for multifunctional sensing as both a manufacturing and *in situ* structural sensor if integrated into the composite. Although this sensor is demonstrated and validated for composites manufacturing, the sensor may be applied to many other manufacturing processes that involve flow and chemical reactions.

2. Experimental

2.1 Materials and manufacturing

The CNT-based sensor is manufactured based on commercially available materials where fibers in a randomly oriented nonwoven glass fiber mat are coated with a thin CNT nanocomposite layer using a straightforward dip-coating process. The nonwoven fabric acts as a carrier for the CNT sensor network. The fabric carrier is an E-glass nonwoven fabric composed of randomly oriented short (12 mm long) chopped fibers held together with a poly vinyl alcohol binder (20103A Technical Fiber Products, Inc.). The areal weight of the fabric is 50 g/m^2 and has a dry sheet thickness of 0.42 mm. The CNT-based sensing fabric was manufactured following a one-step dip-coating process described in our previous work [45,51,56,57]. An aqueous CNT-based dispersion (SIZICYL^{TM} XC R2G, Nanocyl) containing about 1.5 wt% CNT, 3 wt% sodium dodecyl benzene sulfonate surfactant, and 1.5 wt% film former was diluted with ultrapure water at a weight ratio of 1:2 (sizing:H_2O). To ensure a uniform dispersion, the diluted mixture was processed at 2000 rpm

for 2 minutes using a centrifugal mixer (THINKY® ARM-310) followed by 20 min of bath sonication (Branson® 1510). The nonwoven glass fabric was then dipped into the CNT dispersion for 15 minutes followed by drying in a convection oven at 160°C for 1 hour. After drying, a nanocomposite film composed of CNTs in a matrix of the film former and surfactant are left on the surface of the fibers. The fabric was weighed before and after the dip-coating process, and the concentration of the coating on the as-manufactured sensor is approximately 5.5 wt%. For each configuration for composites manufacturing, described in later sections, the fabric sensor was cut to the desired size and electrodes were applied directly to the surface of the fabric using silver paint (SPI Flash Dry Structure Probe, Inc.). For electrical measurements of the sensor response, solid copper wires were attached to the electrodes using a silver-filled conductive epoxy adhesive (EPOXIES® 40-3900, Epoxies, Etc.).

All composites were manufactured using the VARTM technique. For the flow and elevated temperature cure experiments, unidirectional E-glass cloth (2441 g/m^2, Saertex, LLC) was infused under vacuum with a bisphenol-f epoxy mixed with an aromatic amine (EPON 862/EPIKURE™ W, Momentive Specialty Chemicals Inc.) at a mass ratio of 100:26.4 (862:W). For spatial flow mapping using EIT, a plain weave E-glass fabric (3051 g/m^2, Northern Composites) was infused with the same epoxy resin (EPON 862) but a diethylenetriamine curing agent (EPIKURE™ 3223, Momentive Specialty Chemicals Inc) mixed at a ratio of 100:12 was selected to enable room-temperature curing. Prior to infusion, all mixtures were degassed under vacuum for 15 minutes. Major consumables for VARTM, including vacuum bag, peel ply, release film, distribution media, and spiral-cut tubes, were purchased from Coast-Line International (Amityville, NY). Specific experimental configurations for VARTM are discussed in the following sections.

2.2 Materials characterization

Scanning electron microscopy (SEM) was used to characterize the CNT-based textile sensors. SEM micrographs were acquired with an AURIGA™ 60 Crossbeam™ FIB/SEM at an accelerating voltage of 3 kV. To minimize charging, a thin layer of Au/Pt was coated onto the surfaces of the specimens using a vacuum sputter coater (Denton Desk IV, Denton Vacuum LLC) prior to imaging.

For validating polymer transitions, the rheological properties of the EPON 862/EPIKURE W epoxy resin system was characterized using a rheometer (AR-2000, TA Instruments) with a

parallel plate fixture (25-mm diameter, 500-µm gap setting). Oscillatory shear flow tests were conducted with a shear rate of 5 s^{-1} at 1 Hz under the same temperature ramp as the experiments used in curing of the composite at elevated temperatures (temperature ramp at 3°C/min) controlled in the rheometer environmental test chamber.

2.3 In situ VARTM process monitoring with distributed CNT-based textile sensors

The first goal of this work was to validate and demonstrate the performance of the CNT-based textile sensors for flow and cure monitoring in the VARTM composites manufacturing process. Fig. 1a shows a photograph and illustration of the experimental configuration where 6 layers of unidirectional glass fabric is used as the preform for the composite and the resin inlet is to the left in the photograph and the vacuum vent to the right, promoting 1-D flow through the fiber preform. Six unidirectional glass fiber layers were cut to dimensions of 29 cm x 15 cm, and the preform was sealed in a vacuum bag with a layer of impermeable release film on the bottom side between the preform and the tool plate and a layer of permeable peel ply between the preform and the vacuum bag. Near the resin inlet and above the peel ply a highly permeable layer, known as distribution media, extending 10.5 cm was used to accelerate the resin flow across the top of the preform, creating a lag between the flow front at the top and bottom of the glass fiber preform.

In order to track the flow front position on the top and bottom of the fiber preform, two sensors (28 × 7 cm) were integrated in an offset configuration, as shown in Figs 1a and 1b. The sensors were offset so that the position of the flow front on the top and bottom sensor could be visually observed and measured with a digital video camera (Gopro® HERO5 camera, 1080p at 30 fps). For quantitative measurements of the flow location using digital video, a calibration image was taken of a measurement scale with the camera in the same position. The bottom sensor was placed between the release film and the glass fiber preform and the top sensor was placed between the glass fiber preform and the peel ply. As shown in Fig. 1b, each CNT-based textile sensor has five electrodes spaced from edge-to-edge with an electrode spacing of 7 cm creating four local sensing regions in the distributed network on each sensor. The bulk electrical resistance of the sensor can be measured from edge-to-edge and the local resistance changes in each region. Figure 1b shows these measurements and the nomenclature for each local section numbered from left to right with T and B indicating the top and bottom sensors, respectively.

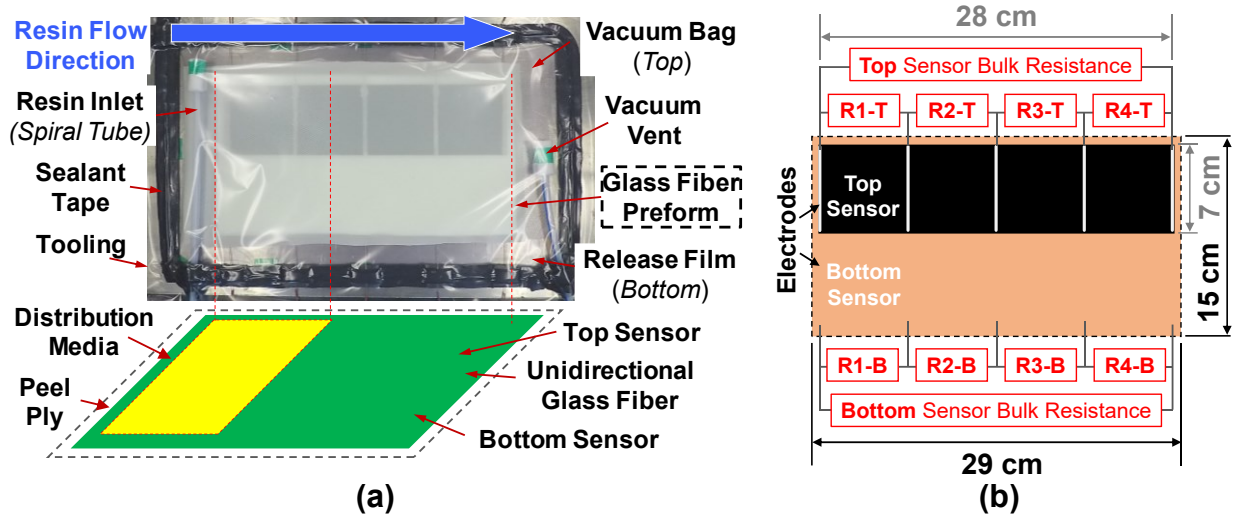

Fig. 1. (a) The VARTM setup with a 1-D resin flow condition (the part preform detailed in the bottom schematic) and (b) the associated sensing scheme of the embedded top/bottom CNT-based area sensors, with each having four distributed sensing regions.

The VARTM manufacturing process involves four distinct stages, including vacuum debulking, resin infusion, curing, and post-curing. Throughout these stages the sensing response was measured in real-time by rapidly multiplexing electrical measurements (Keithley 3706A System Switch/Multimeter) across each sensor by sourcing a constant current of 10 mA and measuring the resulting voltage at electrode locations on the sensor. A customized LabVIEW program was used to synchronize and record electrical measurements. The initial resistance (R_0, at 22°C measured before vacuum application) of each of the eight sensing locations varied from 1475 to 1598 Ω, resulting in an average initial volume resistivity, ρ_0, calculated as 1.55 (±4%) Ω-m. The resistive response of sensors, defined as the percentage change in resistance at any given time, where the resistance change, ΔR, is the measured resistance relative to the initial resistance (R-R_0) and normalized by the initial resistance.

After the fiber preform, sensors, and other process materials were arranged in the proper configuration on the mold, the materials were sealed in a vacuum bag using sealant tape. Vacuum was then applied and the preform was debulked for 5 min. Next, the degassed EPON 862/EPIKURE W epoxy resin mixture was introduced from the inlet to infuse the epoxy into the glass fiber preform. After complete infusion, the resin inlet was closed and the assembly was placed in a convection oven to cure. The oven was heated at 3°C/min to a 135°C and held for 6 h followed by naturally cooling down to room temperature. As a reference, sensors that were not impregnated with epoxy were also subjected to the same temperature cycle to measure their

resistive response with temperature. A type K thermocouple was attached to the surface of the vacuum bag surface to monitor the temperature of the composite. After cooling, the composite was then post-cured for 2.5 h at 170°C.

2.4 Tomographic imaging approach

The second goal of this work was to establish the spatial flow mapping capability of the CNT-based sensing fabric with the integration of a tomographic imaging approach, EIT. The physical model for EIT is derived from the Maxwell's equation that defines the relationship between the conductivity distribution (σ) inside a linear isotropic domain (Ω) and voltages (u) [42,58], given by Eq. (1) with assumption of no interior current source.

$$\nabla \cdot (\sigma \nabla u) = 0 \text{ (in 2D } \Omega) \tag{1}$$

This equation is solved as a forward problem that finds the domain voltages for given current injections with an initial conductivity estimate. The boundary conditions follows the so-called complete electrode model (CEM) [58-60]. Finite element (FE) method is commonly used to numerically compute the weak solution to Eq. (1) by discretizing Ω with triangular elements [42,58]. The FE model is formulated as a linear system of equations given by Equation (2).

$$\begin{bmatrix} A_M + A_Z & A_W \\ A_W^T & A_D \end{bmatrix} \begin{bmatrix} u \\ U \end{bmatrix} = \begin{bmatrix} 0 \\ I \end{bmatrix} \tag{2}$$

where, $[A_M]$ is the usual system matrix for Equation (1); $[A_w]$, $[A_D]$ and $[A_z]$ set CEM boundary conditions [42,58].

The computed nodal voltages $[u]$ are used to build the Jacobian matrix $[J]$ that correlates the boundary voltages to internal conductivity [42]. Nevertheless, to attain EIT maps of conductivity with the known current injections $[I]$ and boundary voltage measurements $[U]$ is an ill-posed nonlinear inverse problem and involves regularization and linearization [42]. Comparing with the absolute imaging algorithm that relies on a single set of $[U]$ to reconstruct the true conductivity within Ω [42,58], we implemented difference imaging algorithm using two sets of measurements in time (i.e., the baseline $[U_0]$ acquired at the debulking stage before resin infusion and transient $[U_t]$ continuously recorded during infusion process) to exclusively reconstruct the time-varying conductivity changes [45,51]. For resin flow mapping, the difference imaging is more applicable and indicative of the flow front evolution due to the fact that resin flow by its nature is a time-dependent, dynamic phenomenon. In this work, a one-step linear difference imaging algorithm,

called maximum a posterior (MAP) given in Equation (3) [45,46,61], was implemented to reconstruct the map of normalized conductivity changes ([$\Delta\sigma/\sigma_0$]).

$$\left\{\frac{\Delta\sigma}{\sigma_0}\right\} = [(J^T W J + \lambda R)^{-1} J^T W]\left\{\frac{\Delta U}{U_0}\right\} = B\left\{\frac{\Delta U}{U_0}\right\} = BZ \tag{3}$$

where

$$[J]_{ij} = -\int \sum_{i=1}^{2} (\nabla u)_i (\nabla u^*)_j dxdy \tag{4}$$

$$\Delta U = [U_i] - [U_0] \tag{5}$$

[W] is the covariance matrix for voltage measurements; [B] is the reconstruction matrix corresponding to a specific regularization parameter, λ [45,51]; [z] = [ΔU] / [U_0] that collects the normalized difference voltage measurements. Note that the regularization matrix [R] imposes the smoothing to the reconstruction. In this study, [R] is an identity matrix based on the basic Tikhonov's regularization method [42,62]. The degree of smoothing is controlled by λ. To find a stable reconstruction without under- or over-smoothness, the noise figure (NF) metric [61,62] given in Equation (6), was utilized to find the optimal λ (λ_{opt}) as NF is equal to 1 [45,46,51]

$$NF = \frac{SNR_U}{SNR_\sigma} = \frac{(1^t \boldsymbol{Z})\sqrt{N \cdot trace(\boldsymbol{ABW^{-1}B^tA})}}{(1^t \boldsymbol{ABZ})\sqrt{M \cdot trace(\boldsymbol{W^{-1}})}} \tag{6}$$

where, SNR_U and SNR_σ are the signal-to-noise ratios of the voltage measurements and the reconstructed conductivity distribution, respectively; N and M are the numbers of elements and voltage measurements, and [A] is matrix of the area of each element. Here, the final EIT map was executed with the reconstruction corresponding to λ_{opt}.

2.5 2D resin flow mapping via CNT-based fabric sensors with integrated EIT approach

The resin flow mapping methodology was validated by VARTM experiments with different radial vent/injection schemes for 2-D flow. Fig. 2a shows a photograph (top) and side-view schematic (bottom) for 2D inward and outward flow monitoring scenarios. Six layers of the plain weave E-glass fabric were cut to 23 × 23 cm as the composite fiber preform, and a 21.6 × 21.6 cm was centered on the fiber preform. As described in Section 2.3, a layer of non-permeable release film was placed between the preform and the tool plate and a layer of peel ply was placed between the preform and the vacuum bag. The CNT-based sensing layer is located between the non-permeable release film and the fiber preform. A metal through-bag valve (401C, Airtech International Inc.) and a continuous spiral tube surrounding the preform were alternately used as the vent/inlet to create the inward and outward flow. For the inward flow configuration a high

permeability layer was placed below the spiral tube and placed in contact with the edge of the fiber preform to enable the resin to flow uniformly around the edge. For all experiments, the mold was first debulked for 5 min. and then the degassed EPON 862/EPIKURE 3223 epoxy resin system was introduced in the resin inlet. As previously described in Section 2.3, the flow front position was also monitored using a digital video camera.

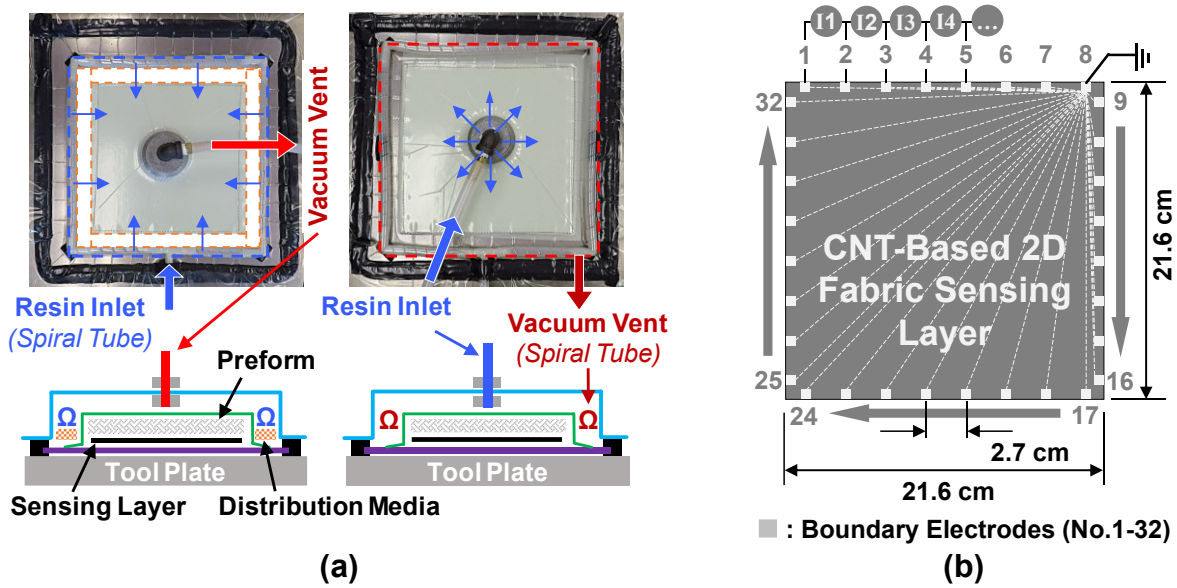

Fig. 2. (a) Experimental configurations for VARTM showing radial vent/injection locations for inward and outward resin flow. (Top) photographs of the experimental showing the location of the resin inlets/outlets and (Bottom) side-view schematic diagram showing the lay-up and location of the sensing layer. (b) The electrical multiplexing approach with 32 boundary electrodes in a hybrid adjacent current-voltage sensing scheme (voltage measurement pathways shown with dashed lines with electrode 8 grounded).

Electrical measurements were taken by applying a set of 32 equidistantly spaced boundary electrodes to the sensor, as shown in Fig. 2b. A customized three-component data acquisition system composed of a sourcemeter (Keithley 6430), multiplexer (Keithley 3706A), and nano-voltmeter (Keithley 2182A) was used to take electrical measurements and supplied constant 10 mA DC injections to electrode pair combinations and measured the voltages around the boundary [45,51,57]. The initial average conductivity was measured in sensor horizontal and vertical directions and used in the forward problem as the *a priori* estimate. EIT measurements were collected using a hybrid adjacent current-voltage scheme employed in our previous work [45,51] and shown in Fig. 2b. In this scheme 32 pairs of current injections (I1 to I32) are consecutively applied to the electrodes, starting from electrode #1, and for each injection the resulting differential

voltages (dashed lines) are recorded with respect to the ground electrode #8, resulting in a single-ended pattern. This 32-electrode sensing scheme avoids overlapping between the pathways of the current injections and voltage measurements. From each EIT data set, 870 independent measurements (= 29 × 30) were used to perform the EIT reconstruction, that is, 29 voltage measurements (without involving the injection electrode pair, i.e., 31-2=29) due to each of the 30 current injections (excluding the two injections with the ground electrode, i.e., 32-2=30). An initial data set was collected prior to resin infusion and then the sequential data sets were continuously recorded until the experiment was complete. Under the previously established EIT framework [45,51,57], the forward FE model meshes the 21.6 × 21.6 cm sensing area with 3454 triangular elements and 1816 nodes that were generated using the DistMesh toolbox [63]. Consistent with our previous work [45], the individual electrode is modeled with a finite length of 3.2 mm with two vertices specified with two adjacent boundary nodes. We adopted the software architecture of the electrical impedance tomography and diffuse optical tomography reconstruction software (EIDORS) [64,65], an open source EIT platform, to calculate the system matrix. Both forward and inverse calculations were handled using MATLAB® software. After collecting each EIT data set, the reconstruction was computed to acquire the EIT map of the resin flow-induced conductivity changes.

3. Results and Discussion

3.1 CNT sensor structure characterization

In this work, the nonwoven glass textile was selected because the fabric acts as a carrier for the carbon nanotube sensing network and allows application flexibility in terms of being able to handle the sensor in a macroscopic form and also being able to conform the sensor to more complex geometries. Following a straightforward dip-coating manufacturing process, this sensor can be easily scaled-up for future applications. The distributed textile sensor has the potential to be used over a large area. For example, in our previous work [57] and as shown in Fig. S1 in Supplementary Information, we demonstrated that we could produce a textile-based sensor in the laboratory on the scale of meters in a few hours. Fig. 3 shows SEM micrographs of the structure of the CNT-based textile sensor across length scales. Fig 3a shows a micrograph of the glass fabric in its as-received state and shows individual fibers randomly oriented in an interconnected network. In some fiber-fiber contact points the poly vinyl alcohol binder is visible (Fig. 3a top right) which

bonds the fiber network together and increases dimensional stability. This type of nonwoven fabric is often used as a veil to improve the surface finish in composite materials, and the fabric has considerable open porosity which enables the liquid resin to readily flow through the fabric. Fig. 3b shows the fabric at a higher magnification in a region where fibers are connected together with the binder and a thin, uniform CNT nanocomposite coating is visible on the surfaces. The CNT dispersion readily wets the surfaces and after drying a continuous CNT nanocomposite sensor network is formed along the fibers [57]. At higher magnifications (Fig. 3c) in a region where the nanocomposite layer has debonded from the fiber surface (rectangle, inset Fig. 3b) the morphology of the nanocomposite coating is visible. The micrograph shows a dense network of entangled carbon nanotubes embedded in the polymer matrix. This dense network of CNTs enables electrically conductive networks to form along the fiber surface. The CNT network electrical conductivity is influenced by CNT-CNT electron tunneling, and this dense network provides a high concentration of contact points in the CNT network where the epoxy polymer matrix can potentially interact with the sensor network to enable the detection of flow and sensing of thermochemical changes in the polymer matrix.

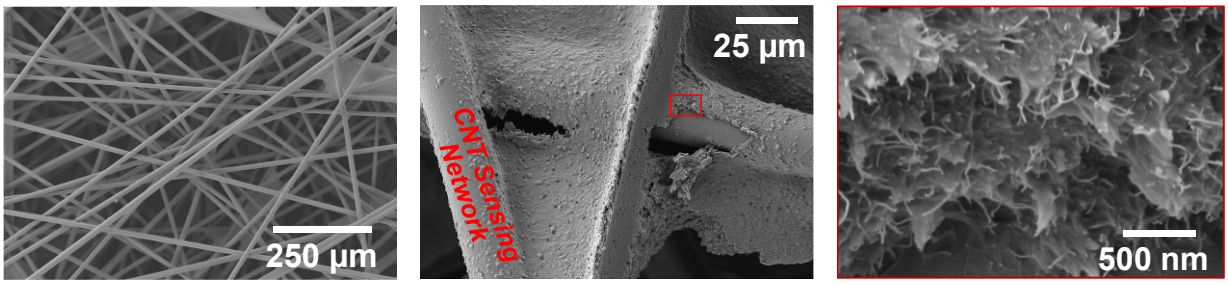

Fig. 3. SEM micrographs showing (a) the as-received randomly oriented nonwoven glass fabric, (b) a crossover region in the fiber network where the binder bridges fiber-fiber junctions with a CNT nanocomposite coating formed via the dip-coating process where an electrically conductive sensor network forms along the fiber, and (c) a high-magnification image of the local CNT sensing layer (rectangular inset in (b)) showing CNTs embedded in the polymer matrix.

3.2 Real-time in situ monitoring of 1-D flow and cure

In order to investigate the response of the CNT-based textile sensor during all stages of the VARTM process, from application of vacuum prior to resin infusion through post-curing, the sensor electrical response was measured continuously throughout the process. As shown in Fig.

1b electrical measurements were taken across the entire length of the sensor and also multiplexed in four local regions across the length of each sensor. Figs. 4a and 4b show experimental data collected during the vacuum debulking and resin infusion segments of the VARTM process for the flow front position measured from video (Fig. 4a) and electrical measurements along the entire length of the sensor (Fig. 4b) aligned on the same time scale for direct comparison. Also shown are the derivatives with respect to time to highlight the flow rate and rate of electrical resistance change. The resin flow front location and global resistance change of the sensor follow the same trends, demonstrating the capability of the distributed sensor to track the position of the flow front using a single measurement. The electrical resistance of the sensor increases as the resin flows through the sensor, resulting in an increase in resistance throughout the infusion process. As the electrically insulating resin flows into the sensing fabric the fiber-fiber contact is likely decreased due to the spring-back effect [6, 66]. In addition, the infiltration of the epoxy may increase the tunneling barrier [36] and disrupt the local tube-tube contacts [39] in the CNT network. During the initial stage of infusion there is a lag between the top and bottom in the flow front due to preferential flow through the high permeability distribution media placed on the top of the preform [7, 10]. Both the flow rate and rate of resistance change are highest at the beginning of the infusion due to this rapid flow through the distribution media. Beyond approximately 40 minutes, the flow and resistance change rates decrease substantially and are nearly the same at the top and bottom of the preform. They decrease linearly until the flow front reaches the end of the preform near the vacuum outlet. There is still a slight lag between the top and bottom for both the flow front position and resistance change as the flow front progresses past the region covered by the distribution media. The lag between the top and bottom decreases as the flow front reaches the vacuum outlet.

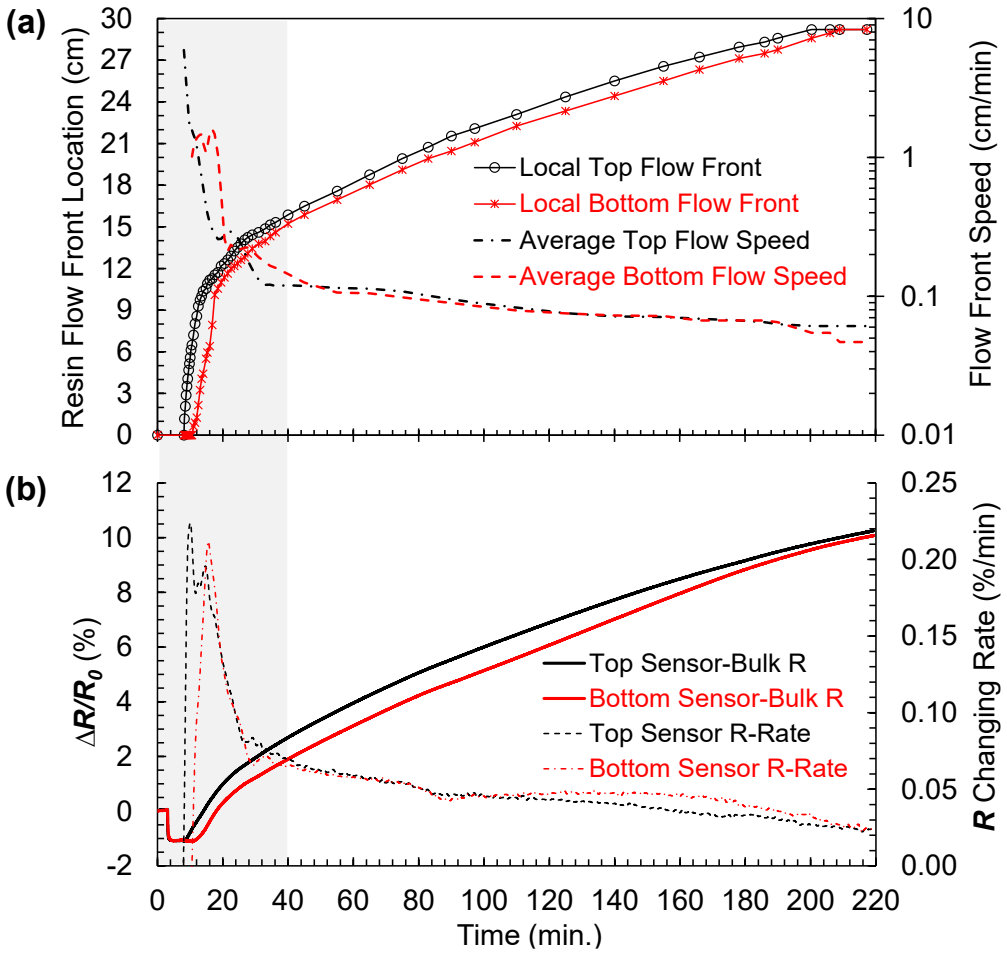

Fig. 4. Experimental data from the 1-D VARTM experiments during the vacuum debulking and resin infusion stages showing (a) the average resin flow position at the top of the preform and the flow rate and (b) the global electrical resistance response and rate of resistance change measured along the entire length of the CNT-based sensor (shaded area shown in Fig. 5).

Figs. 5a and 5b show the flow and electrical response, respectively, during the first 40 minutes of the VARTM process, and Figs. 5c-f shows images of the flow front taken at selected times during infusion. At three minutes after data acquisition was started vacuum was applied to the lay-up. The sensor shows a sharp decrease in the electrical resistance with the application of vacuum as atmospheric pressure on the vacuum bag likely compacts the CNT sensing layer porous network resulting in increased fiber-fiber contact, establishing more conducting pathways and decreasing the overall electrical resistance. One minute after application of vacuum the electrical resistance reaches steady-state.

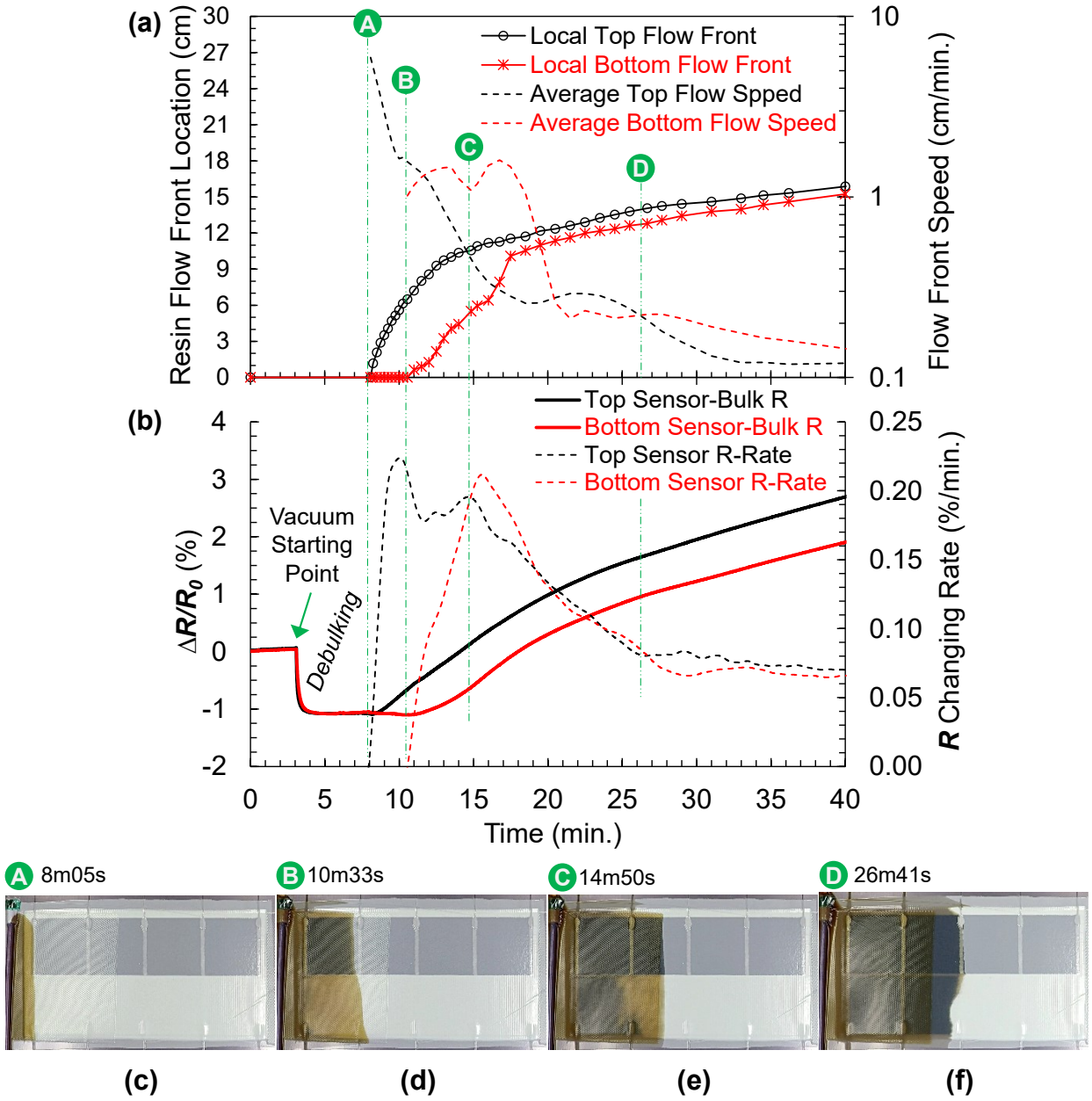

Fig. 5. (a, b) The enlarged view of the experimental data during the first 40 min. of the VARTM process (shaded area of Fig. 4), (c-f) snapshots showing the resin flow front corresponding to the characteristic points A through D.

Five minutes after the application of vacuum the resin is introduced to the vacuum inlet. At point A labeled in the graphs and photographs in Fig. 5, shortly after 8 minutes, the flow front reaches the leading edge of the top sensor and corresponds directly to an increase in the rate of resistance change. In the photographs in Fig. 5c-f the position of the flow front on the top and bottom of the sensor can be tracked visually because the sensors are located in offset positions in

the preform. As seen in Fig. 5d (point B) as the resin flows through the distribution media over the top sensor, the color of the preform is visually dark because the epoxy resin has infiltrated the sensor whereas the color over the bottom sensor is a light brown. As the flow progresses, the resin reaches the bottom of the preform and wets the bottom sensor. When the bottom sensor is wetted with resin, the preform over the bottom sensor also becomes as a dark color, as shown in Figure 5e, which enables us to visually track the position of the flow front on the top and bottom of the preform with the digital camera (data in Fig. 5a). In Fig. 5 at point B (near 10.5 min.) the resin flow reaches the edge of the bottom sensor and the resistance response shows a distinct increase in resistance change rate. At approximately 15 min. in Fig 5d (point C) the flow front at the top reaches the end of the distribution media and the flow at the top of the preform begins to slow down as indicated by the decrease in the flow rate which also corresponds to a local maxima in the rate of resistance change. At this point, there is a clear lag in the flow between the top and bottom sensor. After the flow front extends past the distribution media (Fig. 5, point D) the flow on the bottom of the preform catches-up to the flow on the top as there is no light brown region visible in Fig. 5f. This also corresponds to a stabilizing of the rate of resistance change and flow. There are slight differences in the exact time where the flow and resistance change rates stabilize because the flow rate determined by the digital camera is an average position of the flow front, which is not perfectly straight and likely due to variability in permeability of the glass fiber preform [67].

Fig. 6 shows the flow position and electrical response of the sensor. The sensing response shows a bi-linear trend with an inflection point that corresponds directly to the end of the distribution media. Correspondingly, the flow rate (dashed lines) also shows a sharp decrease when the resin reaches the end of the distribution media. The area sensors show about 1% and 10% increase of resistance change in responding to the fast and slow flow infusion, respectively. This is likely because fast infusion limits resin infiltration into the submicron CNT coating layer in the area sensor. In addition, both the top and bottom sensors show a nearly identical trend of the location-dependent resistance change, suggesting the sensor's repeatability for flow monitoring.

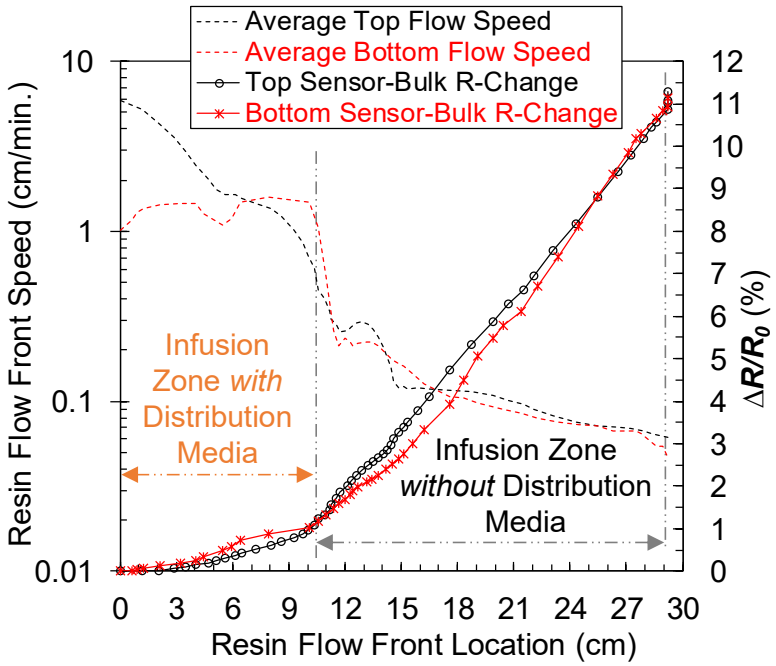

Fig. 6. The relationship between the CNT-based area sensor resistance change and the flow front location compared with the flow rate.

In order to gain additional insight on the local flow progression, the distributed sensing response is further examined in the four distinct sensing regions for the top and bottom sensors, as defined in Fig. 1b (R1-R4). Figs. 7a-d show the transient sensor response in the four sensing regions for the top and bottom sensor and Fig. 7e shows snapshots of the flow progression at selected points of interest indicated on the graph (points E-J). Points A-D from Figure 5 are also shown on the graphs. Figure 7a shows the sensing response in the first region, R1, for the top and bottom sensor. Similar to the global response, there is a sharp increase in resistance change rate at points A and B where the flow reaches the leading edge of the top and bottom sensors, respectively. Near point B there is a local maxima in the resistance change rate of the top sensor, which corresponds to the point where the flow front in the top sensor first reaches the electrode at the end of R1 (Fig. 5d). Similarly, there is also a local maxima in the resistance change rate for the bottom sensor at point C where the flow front first reaches the electrode (Fig. 5e). In the second region, R2 – shown in Fig. 7b, there is also a local maxima of the rate of resistance change of the top sensor at point C, as that location also corresponds to the point where flow at the top of the preform reaches the end of the distribution media. Between points E and F the flow at the bottom of the preform catches-up to the flow front at the top of the preform and at point F in Fig. 7b the resistance change rate for the top and bottom sensor are nearly identical. For the sensing regions that are not

covered by distribution media (R3 and R4, shown in Figs. 7c and 7d, respectively) the resistance changes first when the flow front reaches the edge of the sensing region and the resistance change follows a linear trend from the point where the flow front reaches the first electrode of the sensing region with a relatively constant resistance change rate between electrodes. In these regions the flow front is not completely uniform across the width of the preform, resulting in slight variations in times where the flow front reaches the electrodes for each sensing region.

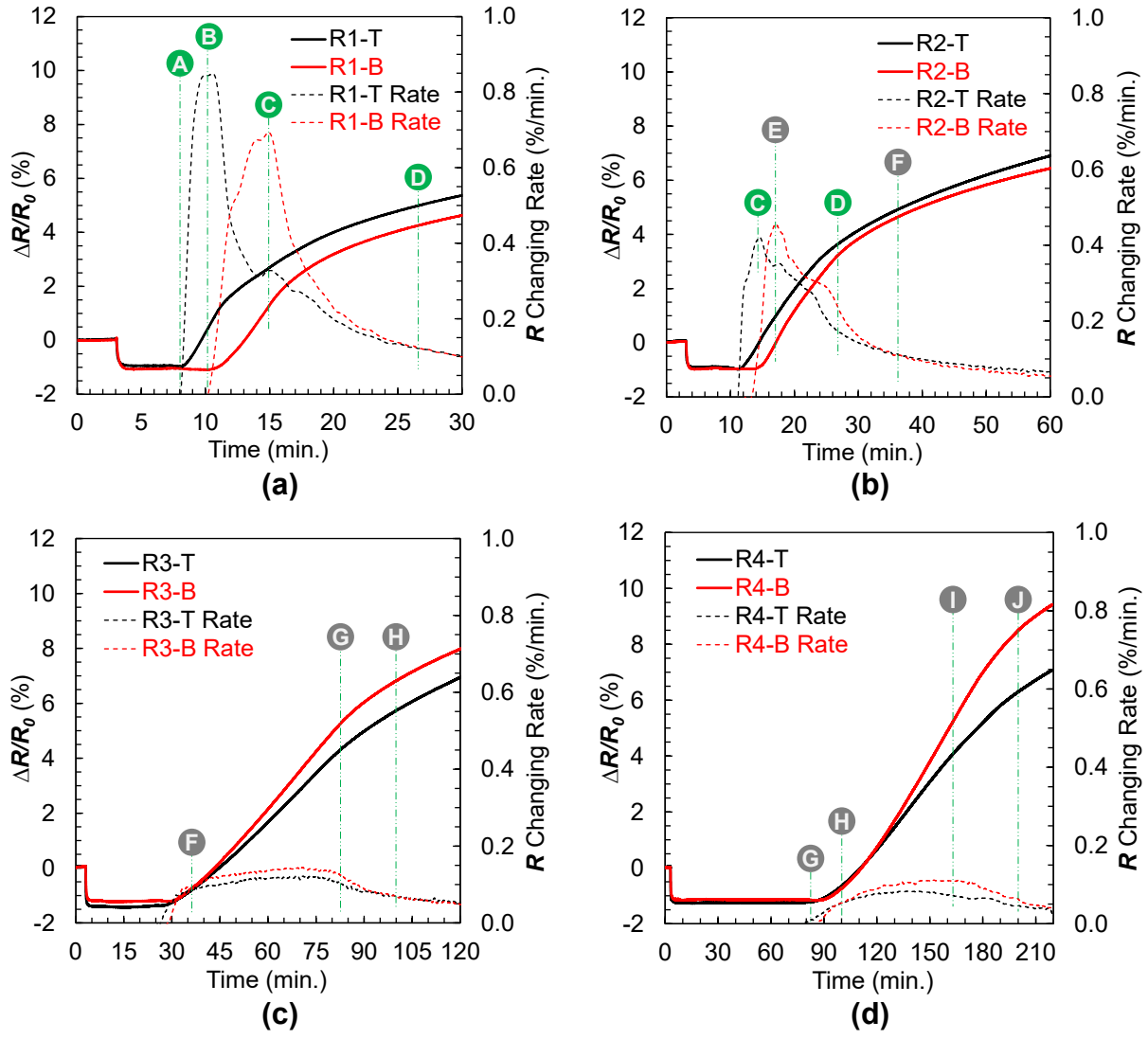

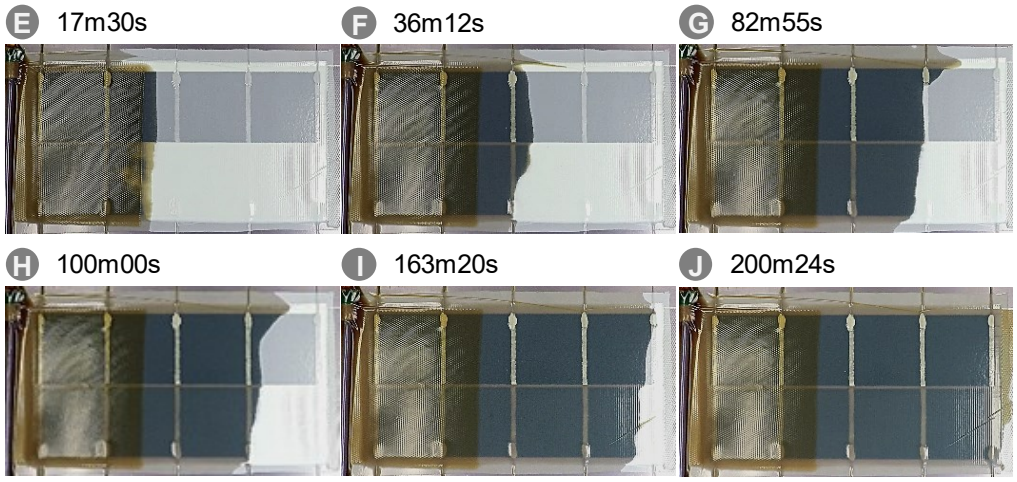

(e)

Fig. 7. (a-d) Resistive responses of the four local distributed sensing regions of the top (T) and bottom (B) sensors from left to right, as defined in Fig. 1b (region #1 to #4), (e) snapshots showing the resin flow front corresponding to characteristic points E through J indicated in the graphs.

After infusion at ambient temperatures was complete, the lay-up was placed into a convection oven to cure the epoxy matrix. Fig. 8a shows the response of the top and bottom sensors during the cure and post-cure temperature cycles. During the initial temperature ramp there is a sharp increase in resistance for both sensors before reaching a peak resistance change of 70-80% during the temperature ramp between 80 and 85°C followed by a decrease and subsequently stabilizing at a constant resistance change during the isothermal segment. Fig. 8b shows the viscosity of the EPON 862/EPIKURE W subjected to the same cure cycle where the temperature is increased at 3°C/min from ambient temperatures to 135°C followed by an isothermal hold. On initial heating the viscosity decreases with temperature but, as the epoxy crosslinks, the viscosity increases. The gel point occurs during the 135°C-isothermal stage, at approximately 64 min. after the minimum viscosity point, where the viscosity drastically increases, indicating the formation of a continuously cross-linked polymer network [68]. The points of minimum viscosity and gelation are indicated on the graph in Fig. 8b. The temperature where the minimum viscosity occurs is near 85°C, which correlates directly with the maximum resistance change observed during the cure cycle. Crosslinking can result in volumetric shrinkage of the polymer matrix and may gradually compress the CNT network [39, 69], possibly causing the resistance decay with increasing viscosity after the maximum during the temperature ramp. The rate of resistance change after the local maximum is also plotted (inset) during the initial cure cycle. As around the same time between the minimum viscosity and gelation, the rate of resistance change approaches zero and

has a rate of resistance change of below -0.008%/min after 62 minutes. This time is also consistent with the time to gelation obtained in the viscosity measurements and suggests that the CNT-based sensor can also be used to monitor curing of the polymer matrix up to the gel point. In addition, during the post-cure cycle the crosslink density of the epoxy matrix increases which may further compress the carbon nanotube network. There is an overall resistance change of -2.6% and -2.0% for the top and bottom sensor, respectively, after post-cure. In order to ensure the changes in the electrical response of the sensor were due to the crosslinking reaction, the sensors were also monitored under vacuum without infusion of the epoxy resin while subjected to the same temperature ramp. Fig. 8c shows the thermal response of the sensor where there is a decrease in electrical resistance with increasing temperature. The response is bi-linear with a 6.5% decrease in resistance over the temperature range as opposed to the large resistance increases associated with curing the epoxy matrix.

For the use of these materials with electrically conductive reinforcements the sensor must be electrically isolated. Here, the sensors are placed in direct contact with the non-conductive glass fiber preform and a non-conductive release film is placed between the sensor and the metal tool. For conductive materials, such as carbon fiber composites, the sensors can be insulated by introducing an isolation layer [70-72]. The sensor may also be used as a sacrificial layer and employed only for process monitoring. The nonwoven fabric can be electrically isolated by placing it above the insulating peel ply laid over the surface of the composite. After curing, the sensor is simply removed along with the peel ply from the composite part. This approach to utilizing the CNT-based fabric as a sacrificial layer is shown in the Supplementary Information (Fig. S2). In addition, the nonwoven fabric layer has high open porosity relative to the peel ply and glass fabric layers and is not expected to alter the flow velocity. These nonwoven fabrics are often used as surface veils to improve the surface finish of composite parts and is a non-structural layer. In case of the CNT-based textile sensor being permanently embedded into the composite after curing for future SHM applications, we expect that this sensor has negligible impact to the overall mechanical performance to the host composite. It has recently been shown that these veils can be interleaved between the layers of structural reinforcement to improve the interlaminar fracture toughness of fiber composites [73].

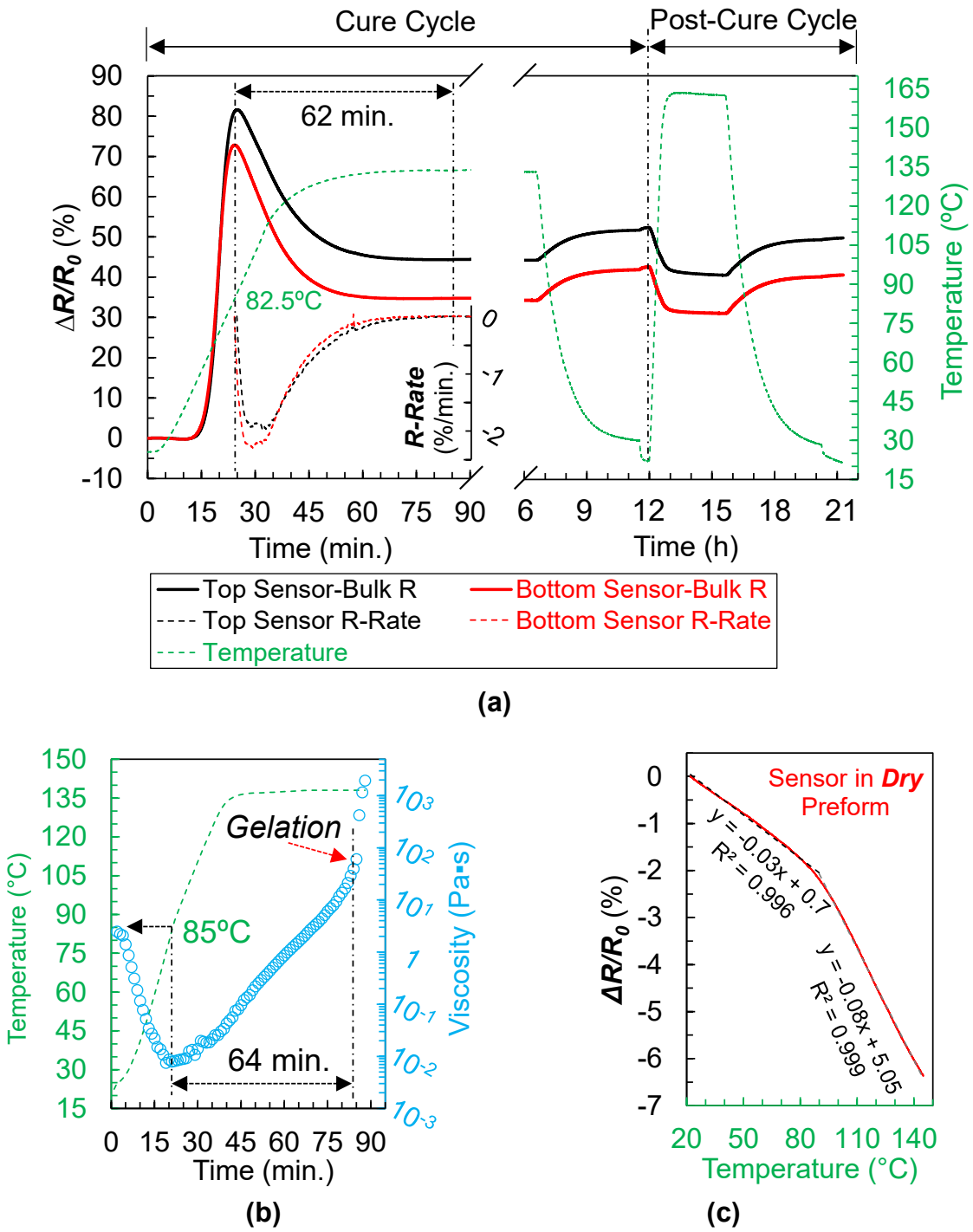

Fig. 8. (a) Sensing response of the CNT-based area sensors during the cure and post-cure stages, (b) an enlarged view of the first 15 min. process in (a), (c) the reference response of the area sensor in the dry preform under full vacuum, and (d) the viscosity profile of the epoxy resin system under the applied heating cure cycle (dashed green line, same as (a)).

3.3 2D spatial flow mapping

While the response of the CNT-based textile sensor has been established under 1-D flow conditions and the position of the flow front can be related to distributed measurements along the length of the sensor, from a practical point of view it is of interest to be able to map the spatial flow for *in situ* process monitoring. In most cases, the geometry of the composite is complex and the injection and vent locations result in 2-D flow within the fiber preform. In addition, complex flow patterns due to varying permeability of the porous fiber preform can result in defects such as dry spots in the final composite part. The efficacy of the sensor to measure flow through electrical changes offers the opportunity to map the conductivity changes of the sensor to monitor the spatial flow progression. The integrated EIT imaging technique handles the collected boundary measurements and generates graphical maps of the resin flow-induced conductivity changes over the sensing area. The EIT method does not require internal electrodes and wiring and is minimally invasive. Four specific cases are examined to determine the feasibility and effectiveness of the EIT approach to detect flow progression as well as defects and dry spots in the final composites. The EIT reconstructions are represented in terms of conductivity, so as resin flows through the CNT-based textile sensor the local resistance of the sensor increases, which corresponds to a decrease electrical conductivity. For all EIT conductivity maps the negative trend in electrical conductivity is represented by the color intensity from dark red, which represents the initial measured electrical conductivity of the sensor prior to infusion, to dark blue.

3.3.1 Inward flow with central vent

In this experiment, the resin was continuously injected through an inlet around the perimeter of the square preform with constant vacuum pressure applied to a vent located directly in the center of the preform. Fig. 9 shows the experimental configuration with the central vent and images taken from video along with corresponding EIT maps at different times during the infusion process. EIT reconstructions were computed with the selected white noise model ([W] in Eq. 3 [45]) and a λ_{opt} of 0.0329. Comparing with the video images, the EIT maps demonstrate accurate estimations to the flow front location (the blue regions from the boundary to the center) and shape (from a square to a circle), demonstrating the feasibility of this methodology for flow mapping. In particular, the EIT maps are plotted in the full scale of the overall reconstructed conductivity changes [-1500%,

400%] to show the evolution of the EIT reconstructions over the resin infusion time, as presented in Supplementary Information, Fig. S3.

Regarding the image quality, it is noticed that all EIT maps presents a 'fringe effect' near the narrow edges, which is likely due to the idealized short electrode model [45] used in this work that could result in the local distortion of the electric field. In particular, the first EIT map in Fig. 9a shows artifacts near the top edge of the infusion, particularly in the upper right-hand corner. This is likely due to measurement errors [74] at the ground electrode (see Fig. 2b) during the initial rapid infiltration around the edge of the preform. As the flow front progresses and reaches steady state, the measurement errors decreased, resulting in EIT maps in Figs. 9b-d with minor background noise. The last two EIT maps, Figs. 9e-f, show a uniform blue background without any features, suggesting full resin infiltration of the preform, and the composite after demolding showed no visible signs of dry spots or voids near the vent. For comparison, the EIT maps generated using an isotropic Gaussian high-pass filter as the smoothing method show reduced overall quality (Supplementary Information, Fig. S7). In addition, consistent with other EIT studies [46], the exaggeration observed in the image amplitudes (represented in terms of conductivity changes) is due to the one-step linear approximation imposed by the MAP algorithm used for the inverse problem. The calculated FE results consisting of the EIT maps are mathematically valid but lacking physical meaning. This limitation can be improved by adding the physical model and constraints related to the resin infusion process in the EIT algorithms and will be explored in future work. Nevertheless, the implemented EIT methodology has successfully demonstrated the spatial location and the relative shape/size of flow front during the entire resin infusion process, validating its feasibility of being a qualitative evaluation tool for process monitoring.

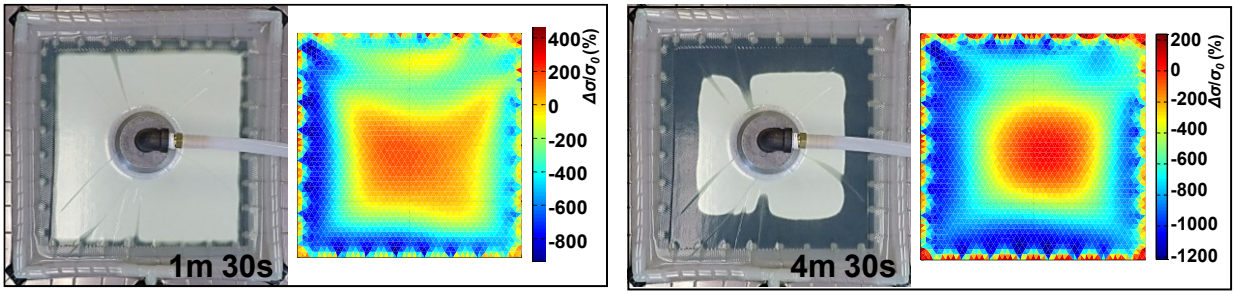

(a) (b)

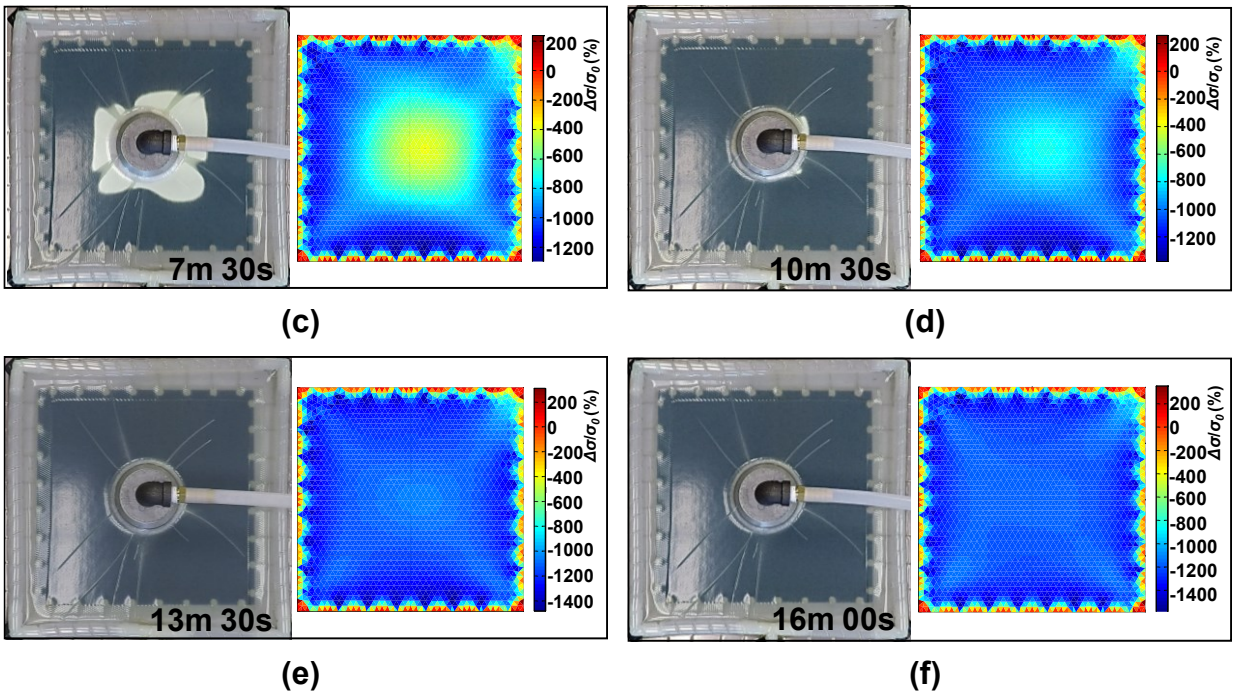

Fig. 9. Experimental results showing (a-f) snapshots showing the resin front locations and shape during the inward flow case with central vent and the corresponding EIT maps showing the resin infused area (blue) and dry region (red) at five consecutive time stamps.

3.3.2 Inward flow with off-center vent

In order to examine the capability of the sensor to detect processing-induced defects, an infusion scheme was designed with a vent offset from the center of the preform so that resin would likely reach the vent prior to complete infusion of the entire fiber preform. In addition, a plastic film (5 cm dia.) was placed just under the through-bag valve to slow-down the infusion so that the resin would likely reach its gel point before complete infiltration, further ensuring the formation of dry spots. Gaussian noise model [46] and a λ_{opt} of 8.97×10^{-8} were used in the EIT inverse calculations. Examining the video images in Figs. 10a-d, the flow front gradually changed from a centered square to an off-centered irregular shape. The corresponding EIT maps shown in Figs. 10a-d, show sharp contrast and accurately map the progression of the flow front. The final EIT map, Fig. 10e, shows a low amplitude oval-like region at the location of the valve, which accurately represents the resin-starved region with multiple dry spots (highlighted in red) that are visually observed after demolding the cured composite (Fig. 10f), demonstrating the effectiveness of the EIT methodology for mapping local infusion defects. Note that the complete set of seven consecutive EIT maps plotted in the full scale of the overall reconstructed conductivity changes [-

1700%, 600%] are shown in Supplementary Information, Fig. S4, demonstrating the smooth evolution of the EIT reconstructions over the resin infusion time.

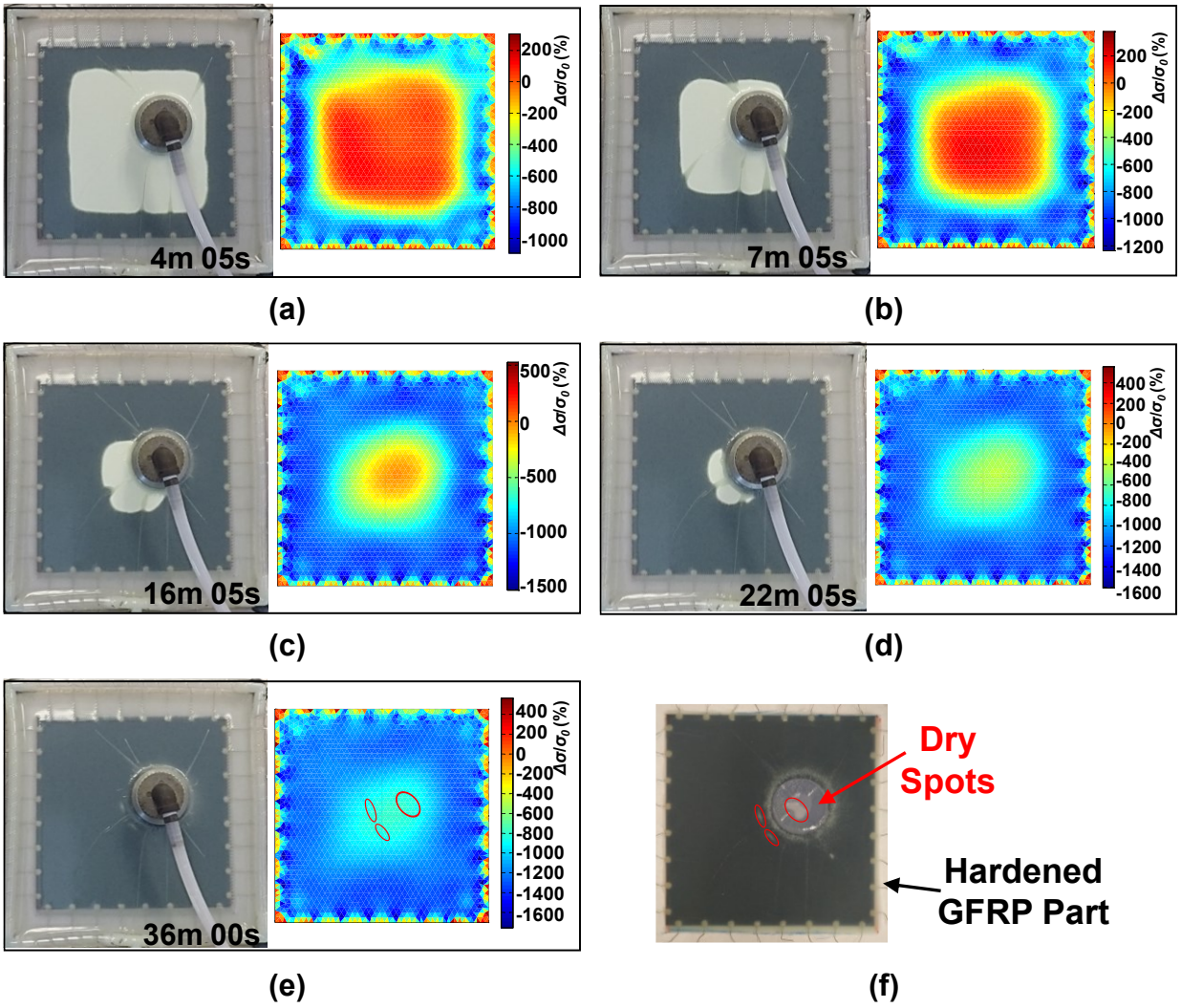

Fig. 10. Experimental results showing (a-e) snapshots showing the resin front locations and shape during the inward flow case with off-center vent and the corresponding EIT maps showing the resin infused area (blue) and dry region (red) at five consecutive time stamps; (f) photograph showing the dry areas in the cured composite.

3.3.3 Complete outward flow infusion with central inlet

In order to examine the capability of the EIT technique to image flow where the resin is not in contact with the boundary electrodes, the direction of the infusion was reversed so that the inlet for the epoxy resin is through the centered through-bag valve and vacuum was applied continuously around the perimeter, resulting in an outward radial flow. From the video images in

Fig. 11, it is observed that some wrinkles in the vacuum bag created local channels for resin flow that resulted in racetracking effects, where resin preferentially flows in areas of low permeability (Fig. 11b) [57], and distorted the overall flow front pattern slightly from an ideal radial flow (Figs. 11c,d). Additionally, small dry areas appeared in corners of the preform, as shown in Fig. 11f, particularly in the lower left-hand corner. For the EIT results, based on the selected white noise model and a relatively large λ_{opt} of 0.039, the EIT maps show a low level of background noise and a relative high degree of smoothing seen as the gradual color transition between the blue zone (resin saturated region) to the red background (dry region). Overall, all EIT maps closely estimate the flow front location and shape. In particular, the low amplitude (light blue) regions in the last EIT map in Fig. 11f closely matches the dry areas in the corners, indicating good sensitivity of this methodology to local infusion variation. It is clear that the overall reconstructed conductivity changes in the range of [-3000%, 1000%] are significantly larger than the EIT results presented in previous two tests, which is believed to be caused by the inter-batch variations among the CNT-based textile sensors' conductivity distributions that could lead to slightly different electrical measurements following the same sensing pattern. A complete set of eight consecutive EIT maps plotted in this full scale is shown in Supplementary Information, Fig. S5. Additionally, we noted that for this specific outward flow application, using an isotropic Gaussian high-pass filter as the smoothing method results in EIT maps with reduced overall quality (Supplementary Information, Fig. S7).

3.3.4 Incomplete outward flow infusion with central inlet and racetracking

In order to amplify the racetracking effects and the formation of dry spots around the edge in the outward flow configuration, a test was conducted where wrinkles were intentionally created in the vacuum bag to distort the flow. As shown in Figure 12a, wrinkles were formed from the injection point to the top edge as well as diagonal wrinkles from the top right to bottom left corners. In addition, the flow was restricted at the inlet and outlet to decrease the infiltration rate. As shown in Figs. 12b-d racetracking formed along the bag wrinkles significantly distorted the initial flow front to an irregular oval shape. The EIT maps shown in Fig. 12 were created with the Gaussian noise model and λ_{opt} of 7.52×10^{-8}. As expected because of the restricted flow, the epoxy resin gelled before reaching full infusion, resulting in substantial dry areas around the edge of the composite (Figs. 12e and 12f). It is clear that all EIT maps have sharp contrast with some scattered

boundary noise and show good approximations for the flow front evolution with respect to the variations in both location and shape. In addition, the last EIT reconstruction in Fig. 12e closely predicts the dry areas formed in the part. Note that the complete set of eight consecutive EIT maps plotted in the full scale of the overall reconstructed conductivity changes [-1700%, 1000%] are shown in Supplementary Information, Fig. S6.

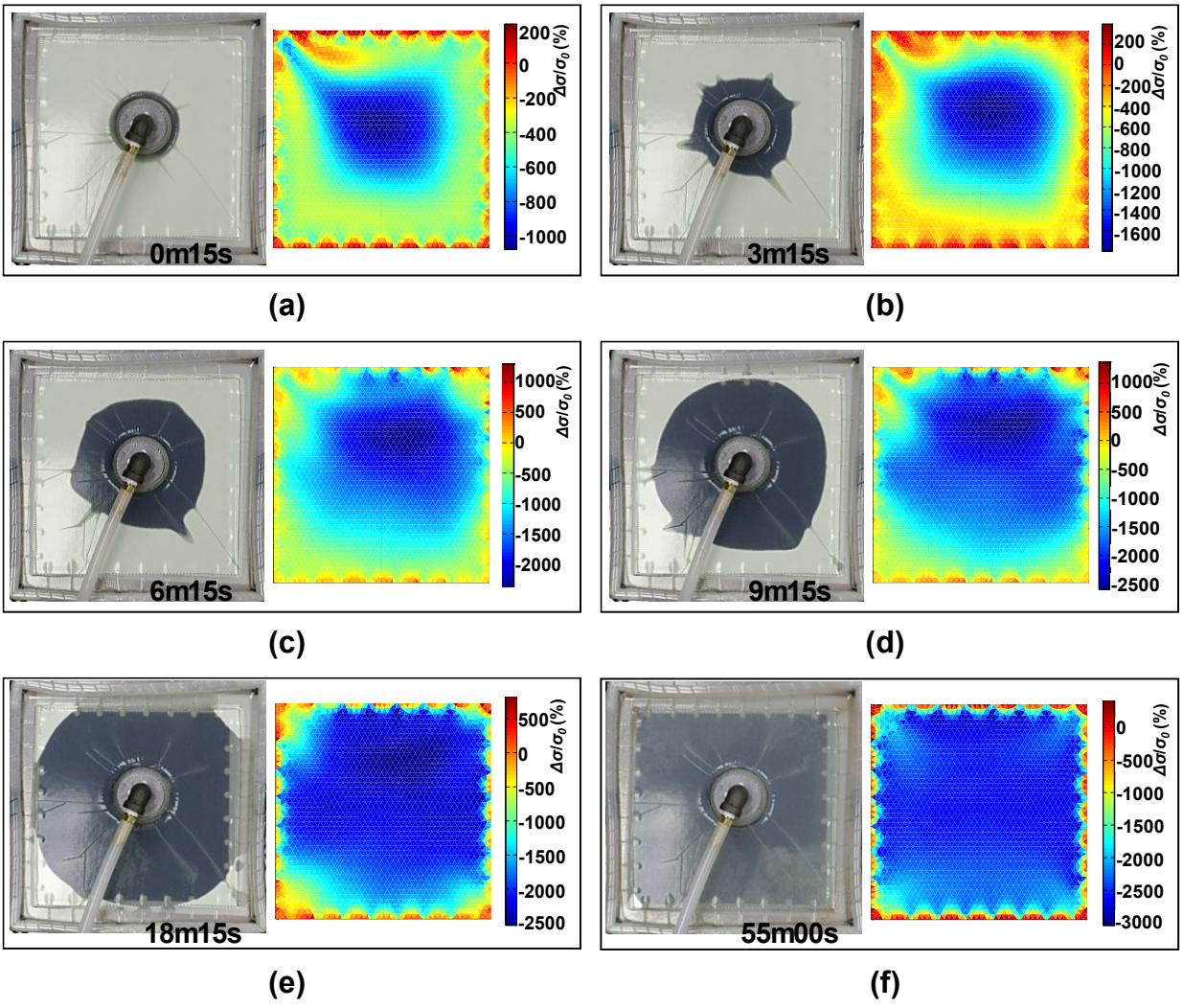

Fig. 11. Experimental results showing (a-f) snapshots showing the resin front locations and shape during the complete outward flow infusion case with central inlet and the corresponding EIT maps showing the dry region (red) and resin infused area (blue) at five consecutive time stamps.

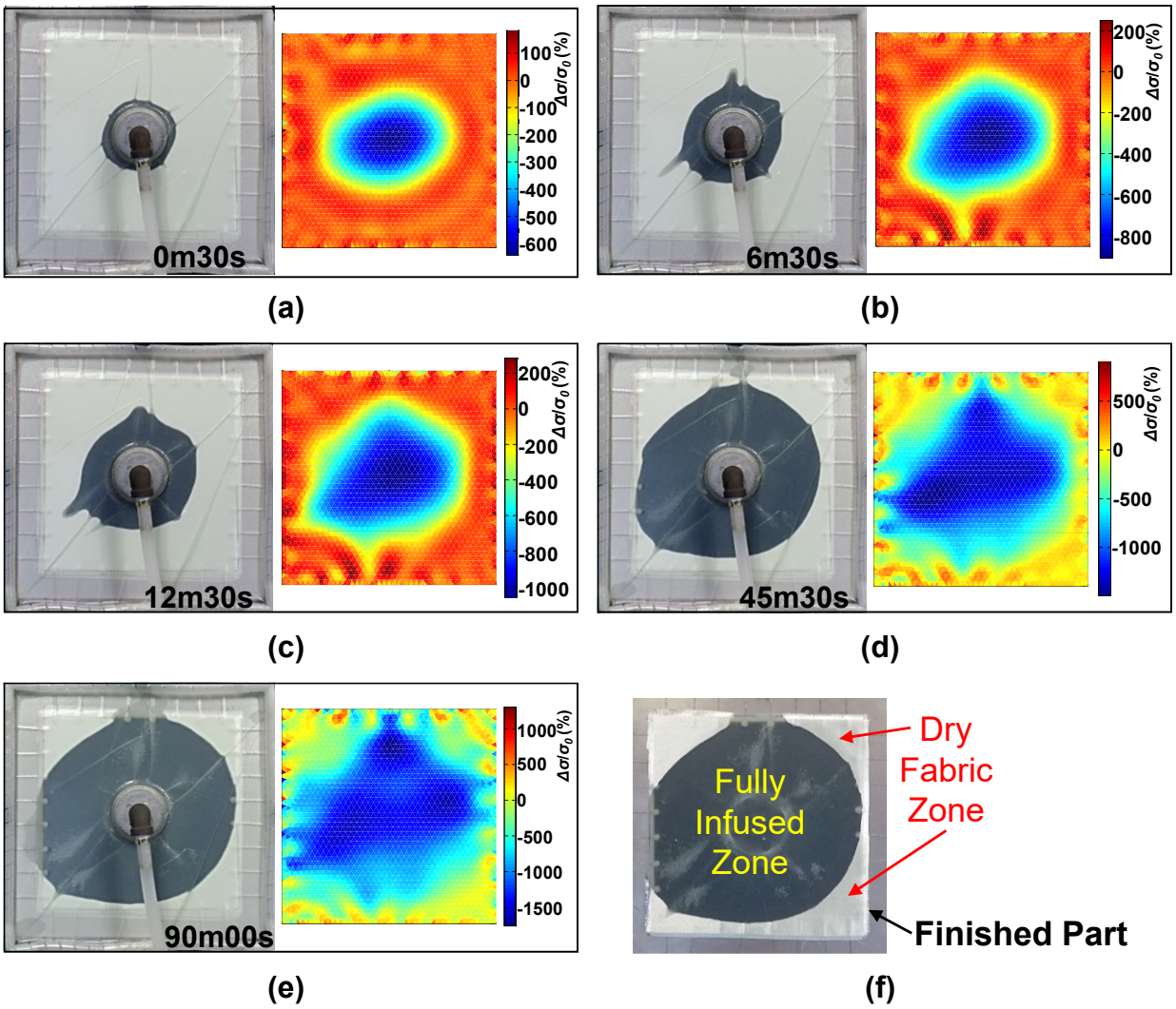

Fig. 12. Experimental results showing (a-e) snapshots showing the resin front locations and shape during the incomplete outward flow infusion case with central inlet and the corresponding EIT maps showing the resin infused area (blue) and dry region (red) at five consecutive time stamps; (f) photograph showing the finished part with large dry fabric zones.

4. Conclusions

In conclusion, we have developed a novel multifunctional sensor where carbon nanotubes are deposited onto a nonwoven glass fiber textile carrier using a scalable dip-coating process. This 400 µm thick sensor is capable of in situ full-field monitoring of the VARTM process. In 1-D flow experiments, the real-time electrical response of the sensor can detect applied vacuum pressure, resin flow progression, and resin phase changes during cure with a bulk gain factor of ~90%. During the infusion process, the insulating epoxy resin drastically decreases the local electrical

conductivity of the fabric by disrupting the carbon nanotube network at the fiber and CNT scales. Compared with the bulk resistive response, the distributed sensing regions partitioned from a continuous sensor show a more immediate and distinguishable response to the local resin flow progression. During the cure cycle the peak of the resistance change response correlates directly with the minimum viscosity during resin cure and when the rate of resistance change reaches zero near the gel point of the epoxy. For the first time, electrical impedance tomography (EIT) has been successfully integrated with this CNT-based fabric sensor during VARTM process to offer true 2-D resin flow mapping capability. In a series of 2-D radial flow experiments, the EIT maps demonstrate accurate estimations for the resin flow, in terms of flow front location and shape, and is able to pinpoint dry spots and unsaturated regions. It is also noted that the periodic EIT maps plotted in the full scale of the overall reconstructed conductivity changes show a smoothing evolution of the EIT reconstructions over the resin infusion time. Solely relying on boundary measurements, this EIT-based method can cover a large sensing area without any internal wiring and electrodes. This type of sensor may be utilized as a tool-mounted sensor that could be removed from the composite after manufacturing but it also offers potential for multifunctional sensing as both a manufacturing and in situ structural sensor if integrated into the composite. Although this sensor is demonstrated and validated for composites manufacturing, the sensor may be applied to many other manufacturing processes that involve flow and chemical reactions.

Acknowledgements

The authors gratefully acknowledge funding from the US National Science Foundation grants 1254540 (NSF CAREER program) and 1827729 (NSF Partnerships for Innovation).

References

[1] Agarwal BD, Broutman LJ, Chandrashekhara K. Analysis and performance of fiber composites. 4th ed. Hoboken NJ: John Wiley & Sons, 2017.

[2] Mallick PK. Fiber-reinforced composites: materials, manufacturing, and design. 3rd ed. Boca Raton FL: CRC Press, 2007.

[3] Irving P, Soutis C. Polymer composites in the aerospace industry. Waltham MA: Woodhead Publishing, 2014.

[4] Guermazi N, Tarjem AB, Ksouri I, Ayedi HF. On the durability of FRP composites for aircraft structures in hygrothermal conditioning. Composites Part B: Engineering 2016;85:294-304.

[5] Advani SG, Hsiao K. Manufacturing techniques for polymer matrix composites (PMCs). : Elsevier, 2012.

[6] Li W, Krehl J, Gillespie Jr J, Heider D, Endrulat M, Hochrein K et al. Process and performance evaluation of the vacuum-assisted process. J Composite Mater 2004;38:1803-1814.

[7] Bender D, Schuster J, Heider D. Flow rate control during vacuum-assisted resin transfer molding (VARTM) processing. Composites Sci Technol 2006;66:2265-2271.

[8] Matsuzaki R, Kobayashi S, Todoroki A, Mizutani Y. Control of resin flow/temperature using multifunctional interdigital electrode array film during a VaRTM process. Composites Part A: Applied Science and Manufacturing 2011;42:782-793.

[9] Bickerton S, Stadtfeld HC, Steiner KV, Advani SG. Design and application of actively controlled injection schemes for resin-transfer molding. Composites Sci Technol 2001;61:1625-1637.

[10] Sas HS, Šimáček P, Advani SG. A methodology to reduce variability during vacuum infusion with optimized design of distribution media. Composites Part A: Applied Science and Manufacturing 2015;78:223-233.

[11] Govignon Q, Bickerton S, Morris J, Kelly P. Full field monitoring of the resin flow and laminate properties during the resin infusion process. Composites Part A: Applied Science and Manufacturing 2008;39:1412-1426.

[12] Di Fratta C, Klunker F, Ermanni P. A methodology for flow-front estimation in LCM processes based on pressure sensors. Composites Part A: Applied Science and Manufacturing 2013;47:1-11.

[13] Tuncol G, Danisman M, Kaynar A, Sozer EM. Constraints on monitoring resin flow in the resin transfer molding (RTM) process by using thermocouple sensors. Composites Part A: Applied Science and Manufacturing 2007;38:1363-1386.

[14] He Y, Li Y, Hao X, Liu S. Micro-flow sensor for continuous resin fluidity monitoring between fibers. Sensors Actuators B: Chem 2019;282:177-186.

[15] Gupta N, Sundaram R. Fiber optic sensors for monitoring flow in vacuum enhanced resin infusion technology (VERITy) process. Composites Part A: Applied Science and Manufacturing 2009;40:1065-1070.

[16] Garschke C, Weimer C, Parlevliet P, Fox B. Out-of-autoclave cure cycle study of a resin film infusion process using in situ process monitoring. Composites Part A: Applied Science and Manufacturing 2012;43:935-944.

[17] Luthy T, Ermanni P. Flow monitoring in liquid composite molding based on linear direct current sensing technique. Polymer composites 2003;24:249-262.

[18] Danisman M, Tuncol G, Kaynar A, Sozer EM. Monitoring of resin flow in the resin transfer molding (RTM) process using point-voltage sensors. Composites Sci Technol 2007;67:367-379.

[19] Yenilmez B, Sozer EM. A grid of dielectric sensors to monitor mold filling and resin cure in resin transfer molding. Composites Part A: Applied Science and Manufacturing 2009;40:476-489.

[20] Matsuzaki R, Kobayashi S, Todoroki A, Mizutani Y. Cross-sectional monitoring of resin impregnation using an area-sensor array in an RTM process. Composites Part A: Applied Science and Manufacturing 2012;43:695-702.

[21] Hegg MC, Ogale A, Mescher A, Mamishev AV, Minaie B. Remote monitoring of resin transfer molding processes by distributed dielectric sensors. J Composite Mater 2005;39:1519-1539.

[22] Kim HG. Dielectric cure monitoring for glass/polyester prepreg composites. Composite structures 2002;57:91-99.

[23] Antonucci V, Giordano M, Cusano A, Nasser J, Nicolais L. Real time monitoring of cure and gelification of a thermoset matrix. Composites Sci Technol 2006;66:3273-3280.

[24] Minakuchi S, Takeda N, Takeda S, Nagao Y, Franceschetti A, Liu X. Life cycle monitoring of large-scale CFRP VARTM structure by fiber-optic-based distributed sensing. Composites Part A: Applied Science and Manufacturing 2011;42:669-676.

[25] Luthy T, Ermanni P. Linear direct current sensing system for flow monitoring in liquid composite moulding. Composites Part A: applied science and manufacturing 2002;33:385-397.

[26] Pandey G, Deffor H, Thostenson ET, Heider D. Smart tooling with integrated time domain reflectometry sensing line for non-invasive flow and cure monitoring during composites manufacturing. Composites Part A: Applied Science and Manufacturing 2013;47:102-108.

[27] Matsuzaki R, Kobayashi S, Todoroki A, Mizutani Y. Full-field monitoring of resin flow using an area-sensor array in a VaRTM process. Composites Part A: Applied Science and Manufacturing 2011;42:550-559.

[28] Vaidya UK, Jadhav NC, Hosur MV, Gillespie Jr JW, Fink BK. Assessment of flow and cure monitoring using direct current and alternating current sensing in vacuum-assisted resin transfer molding. Smart Mater Struct 2000;9:727-736.

[29] England KM, Gillespie Jr JW, Fink BK. Ionic doping of low conductivity structural resins for improved direct current sensing. J Composite Mater 2001;35:1392-1414.

[30] Morais M, Oliva-Avilés A, Matos M, Tagarielli V, Pinho S, Hübner C et al. On the effect of electric field application during the curing process on the electrical conductivity of single-walled carbon nanotubes–epoxy composites. Carbon 2019;150:153-167.

[31] Lu S, Zhao C, Zhang L, Chen D, Chen D, Wang X et al. Real time monitoring of the curing degree and the manufacturing process of fiber reinforced composites with a carbon nanotube buckypaper sensor. RSC advances 2018;8:22078-22085.

[32] Luo S, Obitayo W, Liu T. SWCNT-thin-film-enabled fiber sensors for lifelong structural health monitoring of polymeric composites-From manufacturing to utilization to failure. Carbon 2014;76:321-329.

[33] Luo S, Liu T. Graphite nanoplatelet enabled embeddable fiber sensor for in situ curing monitoring and structural health monitoring of polymeric composites. ACS applied materials & interfaces 2014;6:9314-9320.

[34] Domingues D, Logakis E, Skordos A. The use of an electric field in the preparation of glass fibre/epoxy composites containing carbon nanotubes. Carbon 2012;50:2493-2503.

[35] Zhang J, Zhuang R, Liu J, Scheffler C, Mäder E, Heinrich G et al. A single glass fiber with ultrathin layer of carbon nanotube networks beneficial to in-situ monitoring of polymer properties in composite interphases. Soft Materials 2014;12:S115-120.

[36] Lu S, Chen D, Wang X, Shao J, Ma K, Zhang L et al. Real-time cure behaviour monitoring of polymer composites using a highly flexible and sensitive CNT buckypaper sensor. Composites Sci Technol 2017;152:181-189.

[37] Luo S, Wang G, Wang Y, Xu Y, Luo Y. Carbon nanomaterials enabled fiber sensors: A structure-oriented strategy for highly sensitive and versatile in situ monitoring of composite curing process. Composites Part B: Engineering 2019;166:645-652.

[38] Wang G, Wang Y, Luo Y, Luo S. Carbon Nanomaterials Based Smart Fabrics with Selectable Characteristics for In-Line Monitoring of High-Performance Composites. Materials 2018;11:1677-1688.

[39] Luo S, Wang Y, Wang G, Wang K, Wang Z, Zhang C et al. CNT enabled co-braided smart fabrics: A new route for non-invasive, highly sensitive & large-area monitoring of composites. Scientific reports 2017;7:44056:1-10.

[40] Gnidakouong JRN, Roh HD, Kim J, Park Y. In situ process monitoring of hierarchical micro-/nano-composites using percolated carbon nanotube networks. Composites Part A: Applied Science and Manufacturing 2016;84:281-291.

[41] Ali MA, Umer R, Khan KA, Samad YA, Liao K, Cantwell W. Graphene coated piezo-resistive fabrics for liquid composite molding process monitoring. Composites Sci Technol 2017;148:106-114.

[42] Holder DS. Electrical impedance tomography: methods, history and applications. : CRC Press, 2004.

[43] Harikumar R, Prabu R, Raghavan S. Electrical Impedance Tomography (EIT) and Its Medical Applications: A Review. International Journal of Soft Computing Engineering 2013;3:194-198.

[44] Brown BH. Electrical impedance tomography (EIT): a review. Journal of Medical Engineering & Technology 2003;27:97-108.

[45] Dai H, Gallo GJ, Schumacher T, Thostenson ET. A Novel Methodology for Spatial Damage Detection and Imaging Using a Distributed Carbon Nanotube-Based Composite Sensor Combined with Electrical Impedance Tomography. J Nondestr Eval 2016;35:1-15.

[46] Loyola BR, Briggs TM, Arronche L, Loh KJ, La Saponara V, O'Bryan G, et al. Detection of spatially distributed damage in fiber-reinforced polymer composites. Struct. Health Monit. 2013;12:225-239.

[47] Tallman TN, Wang K. Damage and strain identification in multifunctional materials via electrical impedance tomography with constrained sine wave solutions. Structural Health Monitoring 2016;15:235-44.

[48] Cagáň J, Pelant J, Kyncl M, Kadlec M, Michalcová L. Damage detection in carbon fiber–reinforced polymer composite via electrical resistance tomography with Gaussian anisotropic regularization. Structural Health Monitoring 2019;18:1698-710.

[49] Thomas A, Kim J, Tallman T, Bakis C. Damage detection in self-sensing composite tubes via electrical impedance tomography. Composites Part B: Engineering 2019;177:107276.

[50] Tallman TN, Gungot S, Wang KW, Bakis CE. Tactile imaging and distributed strain sensing in highly flexible carbon nanofiber/polyurethane nanocomposites. Carbon 2015;95:485-493.

[51] Dai H, Thostenson E. Large-Area Carbon Nanotube-Based Flexible Composites for Ultra-Wide Range Pressure Sensing and Spatial Pressure Mapping. ACS applied materials & interfaces, 2019;11:48370-48380.

[52] Tallman T, Gungor S, Koo G, Bakis CE. On the inverse determination of displacements, strains, and stresses in a carbon nanofiber/polyurethane nanocomposite from conductivity data obtained via electrical impedance tomography. J Intell Mater Syst Struct 2017;28:2617-29.

[53] Smyl D, Pour-Ghaz M, Seppänen A. Detection and reconstruction of complex structural cracking patterns with electrical imaging. NDT E Int 2018;99:123-33.

[54] Hassan H, Semperlotti F, Wang K, Tallman TN. Enhanced imaging of piezoresistive nanocomposites through the incorporation of nonlocal conductivity changes in electrical impedance tomography. J Intell Mater Syst Struct 2018;29:1850-61.

[55] Fan G, Gupta S, Loh KJ. Curing and subsurface damage monitoring of epoxy-based composites. Structural Health Monitoring 2019;18:1040-55.

[56] Dai H, Thostenson ET, Schumacher T. Processing and Characterization of a Novel Distributed Strain Sensor Using Carbon Nanotube-Based Nonwoven Composites. Sensors 2015;15:17728-17747.

[57] Dai H. An innovative sensing approach using carbon nanotube-based composites for structural health monitoring of concrete structures. PhD Dissertation, Univeristy of Delaware, United States 2017.

[58] Vauhkonen M. Electrical impedance tomography and prior information. PhD Dissertation, Univeristy of Kuopio, Finland 1997.

[59] Vauhkonen PJ, Vauhkonen M, Savolainen T, Kaipio JP. Three-dimensional electrical impedance tomography based on the complete electrode model. Biomedical Engineering, IEEE Transactions on Biomedical Engineering 1999;46:1150-1160.

[60] Somersalo E, Cheney M, Isaacson D. Existence and uniqueness for electrode models for electric current computed tomography. SIAM J Appl Math 1992;52:1023-1040.

[61] Adler A, Guardo R. Electrical impedance tomography: regularized imaging and contrast detection. Medical Imaging, IEEE Transactions on 1996;15:170-179.

[62] Graham B, Adler A. Objective selection of hyperparameter for EIT. Physiol Meas 2006;27:S65-79.

[63] Persson PO, Strang G. A simple mesh generator in MATLAB. SIAM Review 2004;46:329-345.

[64] Polydorides N, Lionheart WR. A Matlab toolkit for three-dimensional electrical impedance tomography: a contribution to the Electrical Impedance and Diffuse Optical Reconstruction Software project. Measurement Science and Technology 2002;13:1871.

[65] EIDORS: Electrical Impedance Tomography and Diffuse Optical Tomography Reconstruction Software [Online]. Available: http://eidors3d.sourceforge.net/. [Accessed February 10 2020].

[66] Yenilmez B, Sozer EM. Compaction of e-glass fabric preforms in the vacuum infusion process:(a) use of characterization database in a model and (b) experiments. J Composite Mater 2013;47:1959-1975.

[67] Mesogitis T, Skordos AA, Long A. Uncertainty in the manufacturing of fibrous thermosetting composites: A review. Composites Part A: Applied Science and Manufacturing 2014;57:67-75.

[68] Roller M. Rheology of curing thermosets: a review. Polymer Engineering & Science 1986;26:432-440.

[69] Battisti A, Skordos AA, Partridge IK. Dielectric monitoring of carbon nanotube network formation in curing thermosetting nanocomposites. J Phys D 2009;42:155402:1-8.

[70] Ahmed, S., Thostenson, E.T., Schumacher, T., Doshi, S.M. and McConnell, J.R. Integration of carbon nanotube sensing skins and carbon fiber composites for monitoring and structural repair of fatigue cracked metal structures. Composite Structures 2018;203:182-192.

[71] Ahmed, S., Doshi, S.M, Schumacher, T., Thostenson, E.T. and McConnell, J.R. Development of a novel integrated strengthening and sensing methodology for steel structures using CNT-based composites. Journal of Structural Engineering, 2017;143(4):04016202.

[72] Doshi, S.M. and Thostenson E.T., Damage Monitoring of Adhesively Bonded Composite-Metal Hybrid Joints using Carbon Nanotube Based Sensing Layer. Nanocomposites 2020;DOI:10.1080/20550324.2019.1699229

[73] Ognibene, G., Latteri, A., Mannino, S., Saitta, L., Recca, G., Scarpa, F. and Cicala, G. Interlaminar toughening of epoxy carbon fiber reinforced laminates: soluble versus non-soluble veils. Polymers 2019;11(6):1029.

[74] Chitturi V, Farrukh N. Spatial resolution in electrical impedance tomography: A topical review. Journal of Electrical Bioimpedance 2019;8:66-78.